SCIENCE CHINA
Physics, Mechanics & Astronomy

• Article •

March 2022 Vol. 65 No. 3: 235211
https://doi.org/10.1007/s11433-021-1817-8

Edge localized modes suppression via edge $E \times B$ velocity shear induced by RF sheath of ion cyclotron resonance heating in EAST

XinJun Zhang[1], Chu Zhou[2*], XiaoLan Zou[3], TianYang Xia[1], YanLong Li[2], ChengMing Qin[1], XianZu Gong[1], Qing Zang[1], MingHui Li[1], Tao Zhang[4], ShouXin Wang[2], HaiQing Liu[1], Guillaume Urbanczyk[1], Adi Liu[1], YanMing Duan[1], YanPing Zhao[1], JinPing Qian[1], Robert Isaac Pinsker[5], MinYou Ye[2], and BaoNian Wan[1]

[1] *Institute of Plasma Physics, Chinese Academy of Sciences (ASIPP), Hefei 230031, China;*
[2] *School of Nuclear Sciences and Technology, University of Science and Technology of China, Hefei 230026, China;*
[3] *CEA, IRFM, Saint-Paul-les-Durance F-13108, France;*
[4] *Key Laboratory of Optoelectronic Devices and Systems, College of Physics and Optoelectronic Engineering, Shenzhen University, Shenzhen 518060, China;*
[5] *General Atomics, San Diego CA 92186-5608, USA*

Received October 10, 2021; accepted November 22, 2021; published online January 18, 2022

The control of large edge localized modes (ELMs) is a critical issue for the successful operation of future burning plasma devices, such as the international thermonuclear experimental reactor (ITER) and China fusion engineering test reactor (CFETR). In this paper, we present a new active and effective means of ELM suppression using ion cyclotron resonant heating (ICRH) on the experimental advanced superconducting tokamak (EAST). We obtained the key role of the external $E \times B$ velocity shear near the pedestal top and the scrape-off-layer (SOL) induced by the RF sheath potential of ICRH in ELM suppression. The experimental results showed a positive correlation between the RF sheath and the $E \times B$ shear rate in SOL. BOUT++ simulations indicate that increased $E \times B$ velocity shear rates in the pedestal and SOL regions promote ELM suppression; thereby, supporting the experimental observations on EAST. These findings suggest a new simple approach to access the ELM suppressed regimes in plasma with low torque input as ITER baseline discharges.

ion cyclotron resonant heating, RF sheath, edge localized mode suppression, $E \times B$ velocity shear

PACS number(s): 52.30.Cv, 52.35.Py, 52.50.Qt, 52.55.Fa

Citation: X. J. Zhang, C. Zhou, X. L. Zou, T. Y. Xia, Y. L. Li, C. M. Qin, X. Z. Gong, Q. Zang, M. H. Li, T. Zhang, S. X. Wang, H. Q. Liu, G. Urbanczyk, A. Liu, Y. M. Duan, Y. P. Zhao, J. P. Qian, R. I. Pinsker, M. Y. Ye, and B. N. Wan, Edge localized modes suppression via edge $E \times B$ velocity shear induced by RF sheath of ion cyclotron resonance heating in EAST, Sci. China-Phys. Mech. Astron. **65**, 235211 (2022), https://doi.org/10.1007/s11433-021-1817-8

1 Introduction

Sustainment of steady-state high performance plasma is essential in realizing a magnetic fusion reactor energy source. A high confinement mode (H-mode) operation, characterized by a steep edge pressure gradient, is the baseline choice for the current and future tokamak fusion reactors. However, this steep edge pressure gradient can drive repetitive

*Corresponding author (email: zhouchu@ustc.edu.cn)

magneto-hydrodynamic (MHD) instabilities called edge localized modes (ELMs) [1]. ELMs can generate unacceptable transient power loads on the plasma-facing components, which is an enormous challenge for steady-state operation in the international thermonuclear experimental reactor (ITER) and future fusion reactors. Therefore, it is essential to develop the ELM suppression/mitigation techniques or search the alternative stationary ELM-free/small-ELM H-mode regimes for the next step fusion devices. Significant progress has been made over the past decades in the development of ELM controlling physics basis and techniques, such as pellet injection [2], resonance magnetic perturbation (RMP) [3-5], lower hybrid waves [6], and supersonic molecular beam injection (SMBI) [7]. Meanwhile, several alternative stationary ELM- free/small-ELM H-mode regimes have been identified under some conditions, such as the quiescent high confinement (QH) mode with edge harmonic oscillations (EHOs) [8-10], enhanced D_α H-mode (EDA H-mode) [11, 12] and high recycling steady (HRS) H-mode [13] with quasi-coherent mode (QCM) in the pedestal region, and the stationary small ELM H-mode [14, 15]. These technologies or alternative H-mode regimes offer potential solutions. However, they are still insufficient for ELM suppression for future tokamak reactors due to the constraints on the required technical complex and specific conditions with incomplete physics understanding, which remains one of the most active and urgent research topics for ITER.

An active ELM suppression using ion cyclotron resonant heating (ICRH) is first achieved in the experimental advanced superconducting tokamak (EAST) when the RF sheath potential of ICRH is induced at appropriate levels. ICRH is an effective auxiliary heating and current drive tool in the present and next-step devices. The RF sheath of ICRH formed near the antenna and plasma boundary has been extensively studied on many fusion devices with the context of coupling optimization of RF power into plasma and elimination of impurity production [16-30]. Recently, a new ICRH antenna with smaller $k_{\parallel} \sim 7.5$ has been designed, which has a much higher coupling loading while maintaining reasonable good single pass absorption. An impedance transformer close to the antenna is installed, to significantly decrease the transmission line voltage; thereby, allowing higher coupling power. The new ICRH antenna on EAST routinely operates above 1.5 MW and has coupled a maximum power of 2.1 MW (2.4 MW source) into the plasma. The coupling loading and heating efficiency of the new ICRH antenna are ~3-7 times greater than the old B-port antenna [31]. In this paper, we present the study of the radial extension of RF induced Er and its application on ELM suppression through the external $E \times B$ velocity shear on EAST.

Recent theory and experimental evidence show that $E \times B$ velocity shear plays an essential role in the QH mode and ELM mitigation or suppression [32-36]. In the QH mode, simulation and experimental results suggested that strong $E \times B$ velocity shear destabilizes low-n edge harmonic oscillations (EHO), which can enhance edge particle transport; thus, maintaining steady-ELM-free operation regime [35, 37]. Experiments on a lower hybrid current drive (LHCD) and neutral beam injection (NBI) have presented ELM mitigation or suppression accompanied by the increased $E \times B$ velocity shear to reduce the turbulent dissipation by modifying the radial wavenumber spectrum [38] or reducing the linear growth rate of the ballooning mode and shorten its growth time [39]. Moreover, the experiments on ELM suppression using RMPs show that a wide pedestal with suppressed ELMs can experience a transport bifurcation to a staircase structure when the $E \times B$ shear is insufficient to fully suppress long-wavelength electrostatic instabilities [33]. ICRH can effectively change the edge $E \times B$ velocity shear through the induction of RF sheath potential. Thus, it can be used for active ELM mitigation/suppression. To obtain such a possibility and related physics mechanisms, we studied, for the first time, the radial extension of RF sheath induced by ICRF deeply into the core plasma covering the entire pedestal region.

2 Experiments of ELM suppression using ICRH

The evidence of ELM-suppression using ICRH on EAST was first observed in 2016. The recently developed techniques make the control of RF sheath possible, allowing the study of active control of ELMs using ICRH. Figure 1 shows a typical ELM suppression discharge on EAST using the newly developed low $k_{\parallel}$ ICRH antenna [40]. This is a non-torque input RF heated H-mode discharge in the upper single null configuration, with plasma current of $I_p \sim 0.5$ MA, toroidal magnetic field of $B_T \sim 2.5$ T, and edge safety factor of $q_{95} \sim 5.5$; it has 2.2 MW lower hybrid wave (LHW) and 1.0 MW electron cyclotron resonant heating (ECRH) power. The ELM behavior is shown in the D_α time traces in Figure 1(e). The ICRH antenna on B-port was powered on with 0.7 MW at 4.0 s and then reached 1.2 MW at 4.2 s. After injecting ICRH power, the ELM-induced spikes in the D_α emission line disappeared with a slightly decreased emission level, as shown in Figure 1(e). During the ELM suppression, the line-averaged density $\langle n_e \rangle$ increased from 4.0×10^{19} to 4.25×10^{19} m^{-3}, and the plasma stored energy increased slightly, as shown in Figure 1(c) and (d). These observations demonstrate a good feature of the ELM suppression using ICRH without degradation of confinement.

Figure 2 compares the ELM behaviors (D_α light in Figure 2(c1) and (c2)) for two discharges with different RF sheath

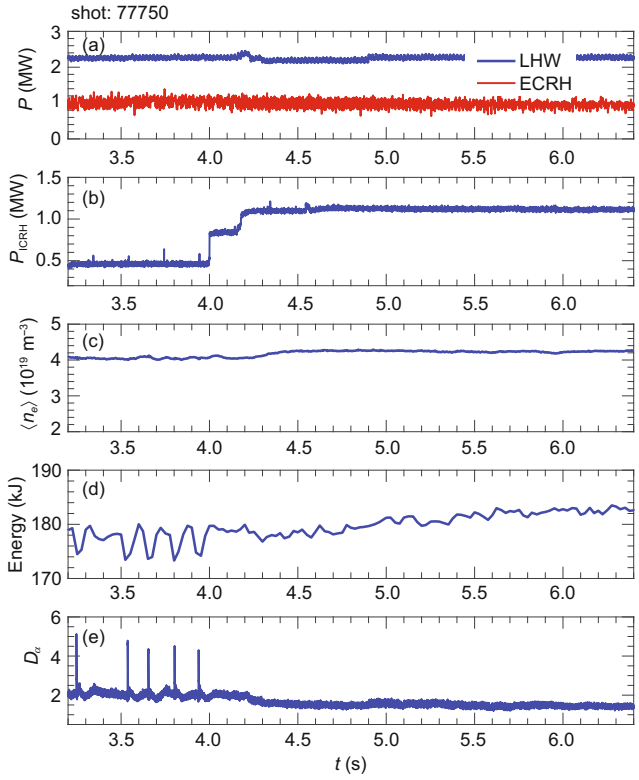

Figure 1 (Color online) Typical discharge for ELM suppressed by ICRH. Time traces of EAST discharge: (a) LHW and ECRH power, (b) ICRH power, (c) line-averaged density, (d) stored energy, and (e) intensity of D_α emissions.

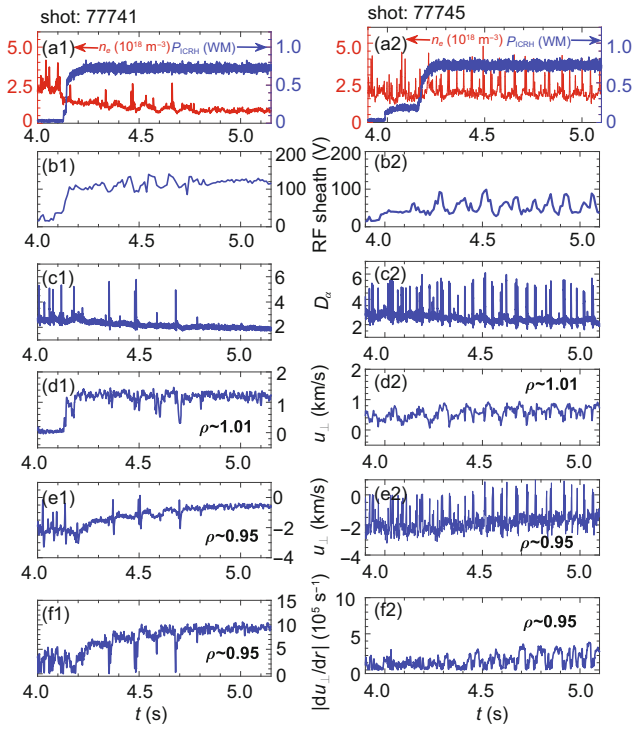

Figure 2 (Color online) Time traces of EAST discharge: (a1), (a2) ICRH on B port; (b1), (b2) RF sheath potential; (c1), (c2) intensity of D_α emissions; (d1), (d2) poloidal velocities in the SOL; (e1), (e2) poloidal velocities near the pedestal top; (f1), (f2) poloidal velocity shear near pedestal top.

potentials induced by ICRH to investigate the impact of RF sheath potentials on ELM suppression. The RF sheath potentials were evaluated from the floating potential profile measured by the Langmuir probe near the ICRH antenna (Figure 2(b1) and (b2)). In these two discharges, the densities near the ICRH antenna (the red lines shown in Figure 2(a1) and (a2)) were different due to different RF sheath potentials. In contrast, all other parameters are similar, including the plasma current of $I_p \sim 0.46$ MA, toroidal magnetic field of $B_T \sim 2.5$ T, central line-average density of $n_e \sim 3.7\times 10^{19}$ m^{-3}, stored energy of ~155 kJ, LHW power of ~2 MW, and ECRH power of ~1 MW. The ELMs show different behaviors in these two shots. The RF sheath potential of ~100 V was induced by ICRH of 0.7 MW at the lower density near the antenna ($n_e \sim 1\times 10^{18}$ m^{-3}) in shot 77741. However, it changed slightly in shot 77745 with a higher density near the antenna ($n_e \sim 2\times 10^{18}$ m^{-3}) at the same ICRH power. It is worth noting that in shot 77745, one of the straps of the ICRH antennas was spuriously triggered around 4 s. Thus, a small ICRH power and RF sheath potential can be observed around 4 s without impacting plasma performance and ELM behavior. In shot 77741, the ELMs were significantly suppressed when the RF sheath potential reached a high stationary level. Meanwhile, the ELM behavior was kept almost unchanged in shot 77745 with a low RF sheath potential. This observation demonstrates the importance of RF sheath potential using ICRH in changing ELM behavior.

Along with the formation of the RF sheath potential, the poloidal velocities in the SOL and pedestal regions were changed in different time scales (Figure 2(d) and (e)), which means a change in external poloidal velocity shear displayed in Figure 2(f). Figure 2(d1), (d2) to (e1), (e2) show the time evolution of the poloidal velocities measured using Doppler backscattering (DBS) [41, 42] at two different radial locations. Here, the positive direction means the ion diamagnetic drift direction. For the DBS system, the measured poloidal velocity $u_\perp$ is the sum of the plasma velocity of the lab frame and the phase velocity of the density fluctuation: $u_\perp = v_{E\times B} + v_{\rm phase}$. At the plasma edge, the phase velocity of turbulence $v_{\rm phase}$ is much smaller than $v_{E\times B}$, meaning $u \sim v_{E\times B}$ [43], and the measured velocity shear is approximately $E \times B$ velocity shear. The velocity shear is derived based on the radial profiles of poloidal velocities, and it is shown in Figure 2(f1), (f2) for the location near the pedestal top. The poloidal velocities in the SOL and pedestal regions changed significantly with an increase in the RF sheath potential in shot 77741; however, they remained almost unchanged in shot 77745 with a small RF sheath potential. In shot 77741, along with the increase of the RF sheath potential, the poloidal velocity in the SOL ($\rho \sim 1.01$ in Figure 2(d1)) increased very quickly in the ion diamagnetic drift di-

rection. In contrast, the poloidal velocities near the top of the pedestal ($\rho \sim 0.95$ in Figure 2(e1)) evolved much slower, suggesting a propagation of the RF sheath potential from SOL to pedestal. The different time evolution of the poloidal velocities at different radial locations increases the poloidal velocity shear, as shown in a selected region near the top of the pedestal in Figure 2(f1). Additionally, the poloidal velocity shear near the top of the pedestal increases before the electron density increase. Figure 3 shows the profiles of electron temperature, density, and poloidal velocity in ELM H-mode before ICRH (the blue lines) and in ELM-suppressed H-mode with ICRH (the red lines) in shot 77741. Thus, the poloidal velocity in SOL ($\rho > 1$) changed significantly during the ELM suppression using ICRH; thereby, significantly increasing SOL velocity shear. Although the poloidal velocity at the bottom of the velocity well decreased slightly, a much narrower velocity well leads to a larger velocity shear near the top of the pedestal.

3 BOUT++ simulation and comparison with experiments

To elucidate the physics of ELM suppression using ICRH, numerical simulations with the BOUT++ framework have been successfully conducted to reveal the nonlinear crash phases of ELMs and energy loss through the three-field two-fluid model [44-46], including the dominant physics of ELMs. The shear flow in the radial electric field strongly affects the turbulence behavior, which can eventually change the energy transport. In these simulations, the $E \times B$ shear rates $\omega_{E\times B}$, which can be calculated using $\omega_{E\times B} = \frac{(RB_\theta)^2}{B}(\frac{\partial}{\partial\varphi})\frac{E_r}{RB_\theta}$ [47], are from the experimental results (Figure 4(a)). The open circles represent the results measured using the DBS system. The fitting solid lines represent the simulations. Figure 4(b) shows the corresponding energy loss ratio by ELM vs. time. The ELM energy loss ratio is defined as follows:

$$\Delta_{\mathrm{ELM}}(t) = \frac{\Delta W_{\mathrm{ped}}}{W_{\mathrm{ped}}} = \frac{\int_{\psi_{\mathrm{in}}}^{\psi_{\mathrm{out}}} \mathrm{d}\psi \oiint J\mathrm{d}\theta\mathrm{d}\varsigma(P_0 - \langle P(t)\rangle_\varsigma)}{(n_e^{\mathrm{ped}}T_e^{\mathrm{ped}} + n_i^{\mathrm{ped}}T_i^{\mathrm{ped}})V_{\mathrm{plasma}}}, \quad (1)$$

where ψ_{in} is the inner boundary of the simulation domain, and ψ_{out} is around the position of the peak pressure gradient; P is the pedestal pressure, J is Jacobian; V_{plasma} is the total plasma volume, and n_e^{ped}, T_e^{ped}, n_i^{ped}, T_i^{ped} are the plasma parameters at the top of the pedestal. The detailed definition and explanation of all quantities in eq. (1) can be found in ref. [44]. The energy loss ratio Δ_{ELM} reduces significantly from the large ELM regime of $> 2.7\%$ to a very small ELM regime of around 0.40% with larger $E \times B$ shear rates in the SOL and near the pedestal top (during ICRH). This is consistent with the experimental observations. The simulation result shows that the enhanced shear flow near the pedestal top can break up the wave packets, resulting in a lower linear growth rate of instability modes, broader mode spectrum, and

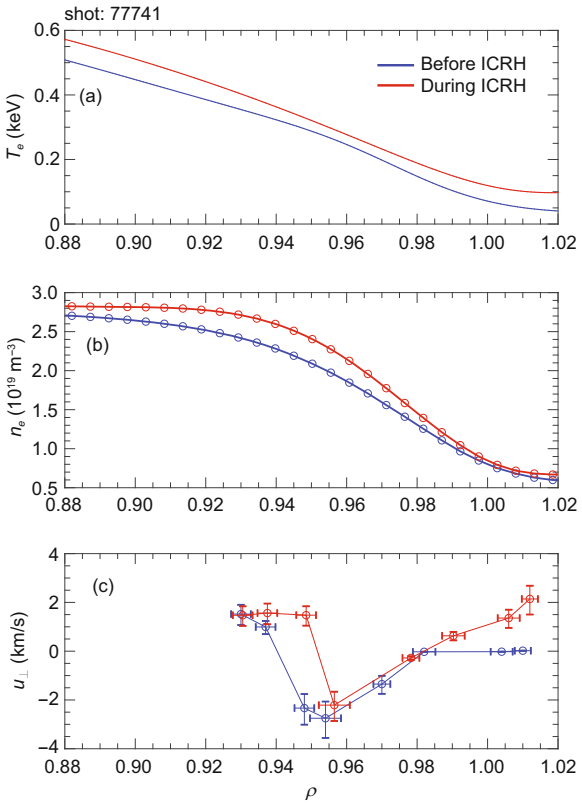

Figure 3 (Color online) Profiles of the electron temperature (a), density (b), and poloidal velocity (c) before and during ICRH.

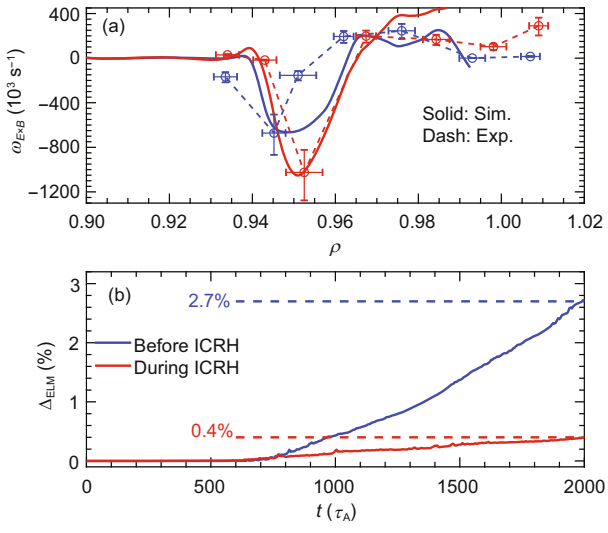

Figure 4 (Color online) (a) $E \times B$ frequency at the outside mid-plane before ICRH (blue curves) and during ICRH (red curves). The solid curves and dashed lines are for simulation and experiment, respectively. (b) ELM size versus time for different $E \times B$ frequencies in panel (a).

longer linear growing phase, as found in ref. [48]. There are more high-n modes coupled, which can effectively compete with the low-n modes for free energy. Strongly nonlinear wave-wave interactions lead to the lack of dominant modes and the decrease in the edge fluctuations. Finally, the large $E \times B$ velocity shear in the SOL can reduce energy loss and further benefit ELM suppression.

As the RF sheath potential induced by ICRH significantly impacts ELMs through the external $E \times B$ velocity shear, establishing the relationship between RF sheath potential and ELM size is essential to develop ICRH as a reliable method for ELM control. A positive correlation between the $E \times B$ shear rate in the SOL and RF sheath potential has been observed in the experiments, e.g., shear rate increasing with the RF sheath potential (Figure 5(a)). Figure 5(b) shows the corresponding ELM sizes versus RF sheath potential from the simulation and experimental observations. The experimental results are from different shots with different RF sheath potential. In accord with the simulation, the experimental ELM sizes are derived from the magnetic perturbation signal, which were used to estimate the energy loss during the ELM crash. The ELMs were mitigated and eventually suppressed as the RF sheath potential increased to a certain level, accompanied by the increase in the $E \times B$ shear rate in the SOL. The simulation results were consistent with the experimental observations, and a threshold value of RF sheath potential was found for ELM suppression. Only above a threshold value can the ELM be suppressed.

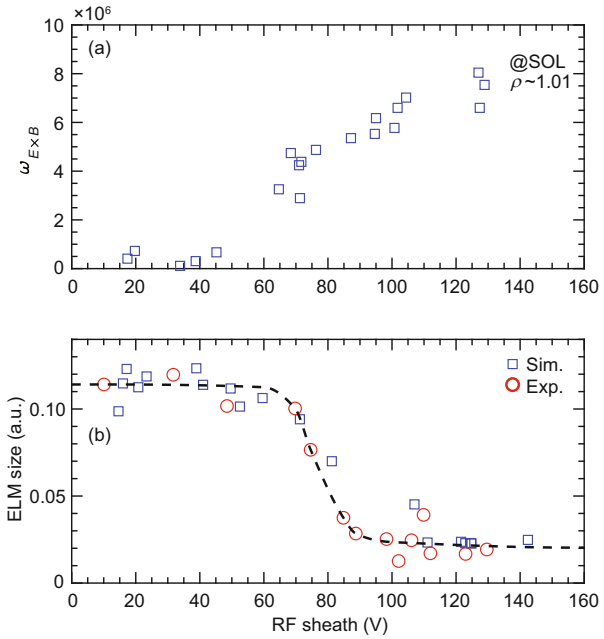

Figure 5 (Color online) Relationship between the $E \times B$ shear rate at SOL and RF sheath potential in experiments (a) and the ELM size versus RF sheath potential from simulations and experiments in EAST (b).

4 Summary

In summary, we have achieved reliably active ELM suppressed H-mode discharges in EAST using a novel and simple technique with ICRH without other mitigation tools. We obtained that the external $E \times B$ velocity shear flow in the SOL and near the pedestal top induced by the RF sheath potential of ICRH has a significant impact on ELMs. A threshold value of the RF sheath potential for ELM suppression was found in experiments and simulations, which were consistent. These novel results present a promising approach to mitigate ELMs for steady-state high-performance plasma operation for future fusion devices.

This work was supported by the National Key Research and Development Program (Grant Nos. 2016YFA0400600, and 2016YFA0400601), the National MCF Energy R&D Program (Grant No. 2018YFE0311200), the National Natural Science Foundation of China (Grant Nos. 11975265, and U1967206), and the Comprehensive Research Facility for Fusion Technology Program of China (Grant No. 2018-000052-73-01-001228). We acknowledge the EAST team for the support of these experiments.

1 J. W. Connor, Plasma Phys. Control. Fusion **40**, 531 (1998).
2 L. R. Baylor, N. Commaux, T. C. Jernigan, N. H. Brooks, S. K. Combs, T. E. Evans, M. E. Fenstermacher, R. C. Isler, C. J. Lasnier, S. J. Meitner, R. A. Moyer, T. H. Osborne, P. B. Parks, P. B. Snyder, E. J. Strait, E. A. Unterberg, and A. Loarte, Phys. Rev. Lett. **110**, 245001 (2013).
3 T. E. Evans, R. A. Moyer, K. H. Burrell, M. E. Fenstermacher, I. Joseph, A. W. Leonard, T. H. Osborne, G. D. Porter, M. J. Schaffer, P. B. Snyder, P. R. Thomas, J. G. Watkins, and W. P. West, Nat. Phys. **2**, 419 (2006).
4 W. Suttrop, T. Eich, J. C. Fuchs, S. Günter, A. Janzer, A. Herrmann, A. Kallenbach, P. T. Lang, T. Lunt, M. Maraschek, R. M. McDermott, A. Mlynek, T. Pütterich, M. Rott, T. Vierle, E. Wolfrum, Q. Yu, I. Zammuto, and H. Zohm, Phys. Rev. Lett. **106**, 225004 (2011).
5 Q. M. Hu, R. Nazikian, B. A. Grierson, N. C. Logan, D. M. Orlov, C. Paz-Soldan, and Q. Yu, Phys. Rev. Lett. **125**, 045001 (2020), arXiv: 1912.06555.
6 Y. Liang, X. Z. Gong, K. F. Gan, E. Gauthier, L. Wang, M. Rack, Y. M. Wang, L. Zeng, P. Denner, A. Wingen, B. Lv, B. J. Ding, R. Chen, L. Q. Hu, J. S. Hu, F. K. Liu, Y. X. Jie, J. Pearson, J. P. Qian, J. F. Shan, B. Shen, T. H. Shi, Y. Sun, F. D. Wang, H. Q. Wang, M. Wang, Z. W. Wu, S. B. Zhang, T. Zhang, X. J. Zhang, N. Yan, G. S. Xu, H. Y. Guo, B. N. Wan, and J. G. Li, Phys. Rev. Lett. **110**, 235002 (2013).
7 W. W. Xiao, P. H. Diamond, X. L. Zou, J. Q. Dong, X. T. Ding, L. H. Yao, B. B. Feng, C. Y. Chen, W. L. Zhong, M. Xu, B. S. Yuan, T. Rhee, J. M. Kwon, Z. B. Shi, J. Rao, G. J. Lei, J. Y. Cao, J. Zhou, M. Huang, D. L. Yu, Y. Huang, K. J. Zhao, Z. Y. Cui, X. M. Song, Y. D. Gao, Y. P. Zhang, J. Cheng, X. Y. Han, Y. Zhou, Y. B. Dong, X. Q. Ji, Q. W. Yang, Y. Liu, L. W. Yan, X. R. Duan, and Y. Liu, Nucl. Fusion **52**, 114027 (2012).
8 C. M. Greenfield, K. H. Burrell, J. C. DeBoo, E. J. Doyle, B. W. Stallard, E. J. Synakowski, C. Fenzi, P. Gohil, R. J. Groebner, L. L. Lao, M. A. Makowski, G. R. McKee, R. A. Moyer, C. L. Rettig, T. L. Rhodes, R. I. Pinsker, G. M. Staebler, W. P. West, and the DIII-D Team, Phys. Rev. Lett. **86**, 4544 (2001).
9 W. Suttrop, V. Hynönen, T. Kurki-Suonio, P. T. Lang, M. Maraschek, R. Neu, A. Stäbler, G. D. Conway, S. Hacquin, M. Kempenaars, P. J. Lomas, M. F. F. Nave, R. A. Pitts, K. D. Zastrow, and the ASDEX Upgrade team and contributors to the JET-EFDA workprogramme, Nucl. Fusion **45**, 721 (2005).

10 N. Oyama, Y. Sakamoto, A. Isayama, M. Takechi, P. Gohil, L. L. Lao, P. B. Snyder, T. Fujita, S. Ide, Y. Kamada, Y. Miura, T. Oikawa, T. Suzuki, H. Takenaga, K. Toi, and the JT-60 Team, Nucl. Fusion **45**, 871 (2005).
11 J. A. Snipes, B. LaBombard, M. Greenwald, I. H. Hutchinson, J. Irby, Y. Lin, A. Mazurenko, and M. Porkolab, Plasma Phys. Control. Fusion **43**, L23 (2001).
12 M. Greenwald, R. Boivin, P. Bonoli, R. Budny, C. Fiore, J. Goetz, R. Granetz, A. Hubbard, I. Hutchinson, J. Irby, B. LaBombard, Y. Lin, B. Lipschultz, E. Marmar, A. Mazurenko, D. Mossessian, T. Sunn Pedersen, C. S. Pitcher, M. Porkolab, J. Rice, W. Rowan, J. Snipes, G. Schilling, Y. Takase, J. Terry, S. Wolfe, J. Weaver, B. Welch, and S. Wukitch, Phys. Plasmas **6**, 1943 (1999).
13 Y. Nagashima, K. Shinohara, K. Hoshino, A. Ejiri, K. Tsuzuki, T. Ido, K. Uehara, H. Kawashima, K. Kamiya, H. Ogawa, T. Yamada, S. Shiraiwa, S. Ohara, Y. Takase, N. Asakura, N. Oyama, T. Fujita, S. Ide, H. Takenaga, Y. Kusama, Y. Miura, and JFT-2M group, Plasma Phys. Control. Fusion **46**, A381 (2004).
14 J. Stober, M. Maraschek, G. D. Conway, O. Gruber, A. Herrmann, A. C. C. Sips, W. Treutterer, H. Zohm, and ASDEX Upgrade Team, Nucl. Fusion **41**, 1123 (2001).
15 G. S. Xu, Q. Q. Yang, N. Yan, Y. F. Wang, X. Q. Xu, H. Y. Guo, R. Maingi, L. Wang, J. P. Qian, X. Z. Gong, V. S. Chan, T. Zhang, Q. Zang, Y. Y. Li, L. Zhang, G. H. Hu, and B. N. Wan, Phys. Rev. Lett. **122**, 255001 (2019).
16 S. J. Wukitch, B. LaBombard, Y. Lin, B. Lipschultz, E. Marmar, M. L. Reinke, and D. G. Whyte, J. Nucl. Mater. **390-391**, 951 (2009).
17 V. Bobkov, M. Balden, R. Bilato, F. Braun, R. Dux, A. Herrmann, H. Faugel, H. Fünfgelder, L. Giannone, A. Kallenbach, H. Maier, H. W. Müller, R. Neu, J. M. Noterdaeme, T. Pütterich, V. Rohde, N. Tsujii, F. Zeus, and H. Zohm, Nucl. Fusion **53**, 093018 (2013).
18 R. Ochoukov, D. G. Whyte, D. Brunner, D. A. D'Ippolito, B. LaBombard, B. Lipschultz, J. R. Myra, J. L. Terry, and S. J. Wukitch, Plasma Phys. Control. Fusion **56**, 015004 (2014).
19 J. Jacquot, D. Milanesio, L. Colas, Y. Corre, M. Goniche, J. Gunn, S. Heuraux, and M. Kubič, Phys. Plasmas **21**, 061509 (2014).
20 J. R. Myra, D. A. D'Ippolito, D. A. Russell, L. A. Berry, E. F. Jaeger, and M. D. Carter, Nucl. Fusion **46**, S455 (2006).
21 D. A. D'Ippolito, and J. R. Myra, J. Nucl. Mater. **415**, S1001 (2011).
22 R. Hong, S. J. Wukitch, Y. Lin, J. L. Terry, I. Cziegler, M. L. Reinke, and G. R. Tynan, Plasma Phys. Control. Fusion **59**, 105008 (2017), arXiv: 1703.07538.
23 I. Cziegler, J. L. Terry, S. J. Wukitch, M. L. Garrett, C. Lau, and Y. Lin, Plasma Phys. Control. Fusion **54**, 105019 (2012).
24 G. Antar, S. Assas, V. Bobkov, J. M. Noterdaeme, E. Wolfrum, A. Herrmann, and V. Rohde, Phys. Rev. Lett. **105**, 165001 (2010).
25 G. Antar, M. Goniche, A. Ekedahl, and L. Colas, Nucl. Fusion **54**, 083018 (2014).
26 M. Bécoulet, L. Colas, S. Pécoul, J. Gunn, P. Ghendrih, A. Bécoulet, and S. Heuraux, Phys. Plasmas **9**, 2619 (2002).
27 D. A. D'Ippolito, J. R. Myra, J. Jacquinot, and M. Bures, Phys. Fluids B-Plasma Phys. **5**, 3603 (1993).
28 D. A. D'Ippolito, J. R. Myra, P. M. Ryan, E. Righi, J. Heikkinen, P. U. Lamalle, J. M. Noterdaeme, and Contributors to the EFDA-JET Workprogramme, Nucl. Fusion **42**, 1357 (2002).
29 J. R. Myra, D. A. D'Ippolito, and M. Bures, Phys. Plasmas **1**, 2890 (1994).
30 S. J. Wukitch, M. L. Garrett, R. Ochoukov, J. L. Terry, A. Hubbard, B. Labombard, C. Lau, Y. Lin, B. Lipschultz, D. Miller, M. L. Reinke, and D. Whyte, Phys. Plasmas **20**, 056117 (2013).
31 X. J. Zhang, C. M. Qin, S. Yuan, H. Yang, Y. S. Wang, Y. Z. Mao, L. N. Liu, L. Wang, Y. P. Zhao, X. Z. Gong, Y. Cheng, X. Deng, K. Zhang, S. Q. Ju, J. G. Li, B. N. Wan, Y. T. Song, W. Zhang, L. Ai, Q. C. Liang, and G. H. Zhu, in *New ICRF antenna Characterization and Performance in EAST: 63rd Annual Meeting of the APS Division of Plasma Physics* (Pittsburgh, 2021).
32 A. Y. Aydemir, Phys. Plasmas **14**, 056118 (2007).
33 A. Ashourvan, R. Nazikian, E. Belli, J. Candy, D. Eldon, B. A. Grierson, W. Guttenfelder, S. R. Haskey, C. Lasnier, G. R. McKee, and C. C. Petty, Phys. Rev. Lett. **123**, 115001 (2019).
34 J. G. Chen, X. Q. Xu, C. H. Ma, P. W. Xi, D. F. Kong, and Y. A. Lei, Phys. Plasmas **24**, 050704 (2017).
35 D. Brunetti, J. P. Graves, E. Lazzaro, A. Mariani, S. Nowak, W. A. Cooper, and C. Wahlberg, Phys. Rev. Lett. **122**, 155003 (2019).
36 P. W. Xi, X. Q. Xu, X. G. Wang, and T. Y. Xia, Phys. Plasmas **19**, 092503 (2012).
37 A. M. Garofalo, W. M. Solomon, J. K. Park, K. H. Burrell, J. C. DeBoo, M. J. Lanctot, G. R. McKee, H. Reimerdes, L. Schmitz, M. J. Schaffer, and P. B. Snyder, Nucl. Fusion **51**, 083018 (2011).
38 G. L. Xiao, X. L. Zou, W. L. Zhong, S. D. Song, X. R. Duan, A. D. Liu, X. Y. Bai, J. Cheng, Z. Y. Cui, L. Delpech, X. T. Ding, J. Q. Dong, A. Ekedahl, B. B. Feng, G. Giruzzi, J. M. Gao, M. Goniche, G. T. Hoang, X. Q. Ji, M. Jiang, B. Lu, D. Mazon, Y. Peysson, X. M. Song, Z. B. Shi, M. Xu, Z. C. Yang, D. L. Yu, B. Y. Zhang, Y. P. Zhang, and Y. Zhou, Nucl. Fusion **59**, 126033 (2019).
39 D. F. Kong, X. Q. Xu, P. H. Diamond, J. G. Chen, C. B. Huang, T. Lan, X. Gao, and J. G. Li, Nucl. Fusion **59**, 016016 (2019).
40 Y. P. Zhao, X. J. Zhang, Y. Z. Mao, S. Yuan, D. Y. Xue, X. Deng, L. Wang, S. Q. Ju, Y. Cheng, C. M. Qin, G. Chen, Y. Lin, J. G. Li, B. N. Wan, Y. T. Song, F. Braun, R. Kumazawa, and S. Wukitch, Fusion Eng. Des. **89**, 2642 (2014).
41 X. Feng, A. D. Liu, C. Zhou, M. Y. Wang, J. Zhang, Z. Y. Liu, Y. Liu, T. F. Zhou, S. B. Zhang, D. F. Kong, L. Q. Hu, J. X. Ji, H. R. Fan, H. Li, T. Lan, J. L. Xie, W. Z. Mao, Z. X. Liu, W. X. Ding, G. Zhuang, and W. D. Liu, Rev. Sci. Instrum. **90**, 024704 (2019).
42 J. Q. Hu, C. Zhou, A. D. Liu, M. Y. Wang, E. J. Doyle, W. A. Peebles, G. Wang, X. H. Zhang, J. Zhang, X. Feng, J. X. Ji, H. Li, T. Lan, J. L. Xie, W. X. Ding, W. D. Liu, and C. X. Yu, Rev. Sci. Instrum. **88**, 073504 (2017).
43 G. D. Conway, J. Schirmer, S. Klenge, W. Suttrop, E. Holzhauer, and the ASDEX Upgrade Team, Plasma Phys. Control. Fusion **46**, 951 (2004).
44 X. Q. Xu, B. Dudson, P. B. Snyder, M. V. Umansky, and H. Wilson, Phys. Rev. Lett. **105**, 175005 (2010).
45 B. Gui, T. Y. Xia, X. Q. Xu, J. R. Myra, and X. T. Xiao, Nucl. Fusion **58**, 026027 (2018).
46 P. W. Xi, X. Q. Xu, and P. H. Diamond, Phys. Rev. Lett. **112**, 085001 (2014).
47 K. H. Burrell, Phys. Plasmas **4**, 1499 (1997).
48 B. Gui, X. Q. Xu, J. R. Myra, and D. A. D'Ippolito, Phys. Plasmas **21**, 112302 (2014).